Received: 27 December 2016 | Revised: 4 April 2017 | Accepted: 4 April 2017

DOI: 10.1002/ajpa.23231

RESEARCH ARTICLE

WILEY American Journal of PHYSICAL ANTHROPOLOGY

Trabecular mapping: Leveraging geometric morphometrics for analyses of trabecular structure

Adam D. Sylvester[1] | Claire E. Terhune[2]

[1]Center for Functional Anatomy and Evolution, Johns Hopkins University School of Medicine, Baltimore, Maryland

[2]Department of Anthropology, University of Arkansas, Fayetteville, Arkansas

Correspondence
Adam D. Sylvester, Center for Functional Anatomy and Evolution, Johns Hopkins University School of Medicine, 1830 E. Monument St., Baltimore, MD 21205 USA.
Email: asylves4@jhmi.edu

Abstract

Objectives: Trabecular microstructure of limb bone epiphyses has been used to elucidate the relationship between skeletal form and behavior among mammals. Such studies have often relied on the analysis of a single volume of interest (VOI). Here we present a method for evaluating variation in bone microstructure across articular surfaces by leveraging sliding semilandmarks.

Methods: Two samples were used to demonstrate the proposed methodology and test the hypothesis that microstructural variables are homogeneously distributed: tali from two ape genera (*Pan* and *Pongo*, $n = 9$) and modern human distal femora ($n = 10$). Sliding semilandmarks were distributed across articular surfaces and used to locate the position of multiple VOIs immediately deep to the cortical shell. Trabecular bone properties were quantified using the BoneJ plugin for ImageJ. Nonparametric MANOVA tests were used to make group comparisons and differences were explored using principal components analysis and visualized using color maps.

Results: Tests reveal that trabecular parameters are not distributed homogeneously and identify differences between chimpanzee and orangutan tali with regards to trabecular spacing and degree of anisotropy, with chimpanzee tali being more anisotropic and having more uniformly spaced trabeculae. Human males and females differed in the pattern of trabecular spacing with males having more uniform trabecular spacing across the joint surface.

Conclusions: The proposed procedure quantifies variation in trabecular bone parameters across joint surfaces and allows for meaningful statistical comparisons between groups of interest. Consequently it holds promise to help elucidate links between trabecular bone structure and animal behavior.

KEYWORDS

bone microstructure, primate behavior, sliding landmarks, trabecular **architecture**

1 | INTRODUCTION

The complex hierarchical structure of bone tissue has been the subject of considerable research, both in terms of bone physiology (e.g., hematopoiesis, mineral homeostasis) (e.g., Raggatt and Partridge, 2010; Teti and Zallone, 2009) and bone mechanics (e.g., stress and strain patterns, bone material properties) (e.g., Burr and Allen, 2014; Currey, 1984; Ruff, Holt, & Trinkaus, 2006). At the macroscopic level, skeletal elements are composed of two basic types of bone tissue, cortical bone and trabecular bone, and there is a long history of work linking the structure of these tissues to mechanical loading regimes. Originally proposed by Julius Wolff (Wolff, 1892), most modern interpretations of his eponymous law are more broadly summarized as "over time, the mechanical load applied to living bone influences the structure of bone tissue" (Cowin, 2001:30-1).

Continued research building upon Wolff's initial work has consistently demonstrated that bone responds functionally to its mechanical loading environment (e.g., Barak, Lieberman, & Hublin, 2011; Bertram and Schwartz, 1991; Biewener, Fazzalari, Konieczynski, & Baudinette, 1996; Chen, Liu, You, & Simmons, 2010; Frost, 1990a,b; Huiskes, Ruimerman, van Lenthe, & Janssen, 2000; Lieberman, Devlin, & Pearson, 2001; Pearson and Lieberman, 2004; Ruff et al., 2006; ; Teichtahl et al., 2015; Woo et al., 1981). Departures from optimum strain level can cause bone deposition (resulting from increased strain) or bone loss

(resulting from decreased strain), and both processes help maintain bone tissue at its optimal strain levels (e.g., Lanyon, 1982). Importantly, these optimal strain levels are not constant across the skeleton (e.g., Lieberman et al., 2001) and can vary in relation to age, health status, genetic background, hormone levels, among other factors (e.g., Frost, 1987, 2003; Glass et al., 2016; Glatt, Canalis, Stadmeyer, & Bouxsein, 2007; Lanyon, 1996; Lieberman et al., 2001; Majumdar et al., 1997; Pearson and Lieberman, 2004). Trabecular bone responds to increased strain by increasing trabecular thickness (Tb.Th), which if the trabecular structure remains otherwise unchanged, will lead to a concomitant increase in bone volume fraction (BV/TV) (Rubin, Turner, Bain, Mallinckrodt, & McLeod, 2001). BV/TV represents the proportion of bone volume within a given volume of interest (VOI). Trabecular bone may also respond via changes in trabecular orientation, where trabeculae may become preferentially oriented parallel to the axis of highest loads (Biewener et al., 1996; Fajardo and Müller, 2001; Goldstein, Matthews, Kuhn, & Hollister, 1991; Lanyon, 1974). Conversely, if strains are below optimum levels, trabecular thickness and bone volume fraction may decrease. The increased metabolic activity and remodeling rate of trabecular bone relative to cortical bone (Eriksen and Glerup, 2000; Eriksen, Mosekilde, & Melsen, 1985) suggests that trabecular bone is more responsive to its mechanical environment than cortical bone and will reflect functional demands during the life of an individual.

A wide variety of studies have sought to employ Wolff's law to elucidate links between bone tissues and animal behavior. Such studies have examined cortical bone cross-sectional properties (e.g., Morimoto, Ponce de León, & Zollikofer, 2011; Patel, Ruff, Simons, & Organ, 2013; Ruff, 2002), subchondral bone apparent density (e.g., Carlson and Patel, 2006), and trabecular bone structure (e.g., Fajardo and Müller, 2001; Fajardo, Müller, Ketcham, & Colbert, 2007; Kuo, Desilva, Devlin, McDonald, & Morgan, 2013; MacLatchy and Müller, 2002; Matarazzo, 2015; Ryan and Ketcham, 2002; Ryan and Shaw, 2012, 2013; Ryan and Walker, 2010; Saparin, Scherf, Hublin, Fratzl, & Weinkamer, 2011; Tsegai et al., 2013). Collectively, this body of work has included a wide variety of primate taxa (e.g., Polk, Williams, Peterson, Roseman, & Godfrey, 2010; Ryan and Shaw, 2013), including bioarchaeological and modern samples of humans (e.g., Chirchir, Ruff, Junno, & Potts, 2017; Ruff, 2008; Ruff and Hayes, 1983; Saers, Cazorla-Bak, Shaw, Stock, & Ryan, 2016), as well as fossil hominins (e.g., Barak et al., 2013; Chirchir et al., 2015; DeSilva and Devlin, 2012; 2015; Hill and Durband, 2014; Ruff, 2008; Skinner et al., 2015; Zeininger, Patel, Zipfel, & Carlson, 2016). These studies have used trabecular bone to answer questions about locomotor patterns (e.g., Ryan and Shaw, 2012), tool use (e.g., Skinner et al., 2015), physical activity levels based on subsistence strategies (e.g., Chirchir et al., 2017), as well as mandibular biomechanics (e.g., Daegling, 1992, 2001, 2007).

Straightforward links between trabecular structure and behavior have, however, remained elusive (DeSilva and Devlin, 2012; Fajardo et al., 2007; Morimoto et al., 2011; Ryan, Colbert, Ketcham, & Vinyard, 2010; Ryan and Walker, 2010). Ambiguous results have prompted some researchers to conclude that various behaviors are not reflected in trabecular bone structure (e.g., Ryan et al., 2010). In some cases, results of trabecular analyses contradict those of cortical bone, even for the same skeletal region, fueling the need for additional research (e.g., Fajardo et al., 2007). There are multiple potential reasons for the equivocality of these results, including mundane issues of sample sizes and taxonomic diversity to more challenging problems of accounting for confounding biological factors (e.g., body size, sexual dimorphism, age, health status). Kivell (2016) points out two major methodological issues in relation to VOI placement and size: (1) VOI size must be large enough to encapsulate enough trabeculae for analysis, but small enough to avoid cortical bone, which is problematic in irregularly shaped and/or small bones; (2) determining where to place VOIs so that they are anatomically and/or biomechanically homologous across individuals is challenging given the wide range of complex morphologies often being considered.

Many previous researchers have approached the study of trabecular structure by analyzing a single VOI per specimen, often placed in the center of the epiphysis of the skeletal element/joint of interest [e.g., Kuo et al., 2013; Ryan and Shaw, 2012; Ryan and Walker, 2010; but see Chirchir, Zeininger, Nakatsukasa, Ketcham, & Richmond, (in press); Griffin et al., 2010; Zeininger, Richmond, & Hartman, 2011; for examples of studies using multiple VOIs]. Although intuitive, this standard methodology may limit inferences about animal behavior. If the VOI is not placed in the trabecular structure where the behavioral signal is detectable (which cannot be known *a priori*), it may appear as if the trabecular structure contains little to no behavioral information. Some researchers have attempted to address these limitations by looking at a few VOIs distributed across a structure (e.g., Chirchir et al., in press; DeSilva and Devlin, 2012; Griffin et al., 2010), or by sequentially moving a single VOI throughout a larger region of interest and analyzing all of the values returned (Saparin et al., 2011). Several methodologies for selecting VOI size have also been employed. Some researchers have used a standard VOI size across specimens (e.g., Fajardo and Müller, 2001; Kuo et al., 2013), while others have advocated for scaling VOI size relative to the structure being examined (e.g., Ryan and Shaw, 2012), or have treated the entire trabecular structure as a single VOI (e.g., Ryan et al., 2010). Analyses examining error related to variation in VOI size and location (Kivell, Skinner, Lazenby, & Hublin, 2011; Lazenby, Skinner, Kivell, & Hublin, 2011) suggest that both variables can significantly influence analytical outcomes, though structural variables (i.e., degree of anisotropy, connectivity) were more sensitive to changes in VOI size than mass variables (i.e., bone volume fraction, trabecular thickness, trabecular number).

To overcome some of these challenges, more recent work by Gross, Kivell, Skinner, Nguyen, & Pahr (2014) describes a method that is capable of evaluating trabecular distributions throughout a single skeletal element. This approach uses finite element techniques to generate a mesh of tetrahedral elements that are then used in combination with a VOI to calculate bone volume fraction and trabecular orientation. VOI size is scaled to be the smallest sphere in which at least four structural features (i.e., trabeculae) are included (Pahr and Zysset, 2009; Gross et al., 2014). Ultimately, this method generates color maps showing the relative distribution of bone volume fraction and

TABLE 1 Sample composition

Species	Sex	Institution	Specimen ID
Homo sapiens	F	UTK	[a]
Homo sapiens	F	UTK	[a]
Homo sapiens	F	UTK	[a]
Homo sapiens	F	UTK	[a]
Homo sapiens	F	UTK	[a]
Homo sapiens	F	UTK	[a]
Homo sapiens	M	UTK	[a]
Homo sapiens	M	UTK	[a]
Homo sapiens	M	UTK	[a]
Homo sapiens	M	UTK	[a]
Pan troglodytes	F	USNM	USNM 176227
Pan troglodytes	F	USNM	USNM 176229
Pan troglodytes	F	USNM	USNM 220062
Pan troglodytes	F	AMNH	AMNH-H-89426
Pan troglodytes	F	AMNH	AMNH-H-89426
Pongo pygmaeus	F	USNM	USNM 142170
Pongo pygmaeus	F	USNM	USNM 142169
Pongo abelli	F	USNM	USNM 143596
Pongo abelli	F	USNM	USNM-M 143697

[a]The University of Tennessee (UTK) identification number are not available for publication.
USNM—Smithsonian Institution National Museum of Natural History.
AMNH—American Museum of Natural History.

trabecular orientation across the morphology in question. This method represents a significant step forward for evaluating variation in trabecular architecture across an entire structure, rather than just a single or handful of VOIs, and has the power to provide more detailed interpretations of trabecular architecture relative to axes of peak loading (Kivell, 2016). One major drawback of this method, however, is its inability to statistically compare trabecular structure across individuals or regions (Gross et al., 2014; Kivell, 2016).

Here we present a new method for examining trabecular variation across an entire articular surface that allows for comparisons among groups of interest by leveraging the flexible geometric morphometric toolkit. The rapid rise of geometric morphometrics (GM) over the past 20 years has provided biologists with techniques to compare complex shapes statistically across a variety of taxa and skeletal elements (e.g., Adams, Rohlf, & Slice, 2013; Cooke and Terhune, 2015). We employ the now common technique of sliding semilandmarks to position multiple VOIs deep to the cortical shell of an articular surface, which allows us to quantify variation in trabecular bone parameters across the entire joint surface. This method combines the power of standard trabecular analytical techniques and variables with an intuitive and replicable way of placing a large number of homologous VOIs across the area of interest. We demonstrate this method for small samples of hominid tali and modern human distal femora. We test the null hypothesis that trabecular bone parameters are homogenous across the joint surfaces examined here. If this null hypothesis fails to be rejected, we would accept that any one VOI could be used to quantify the trabecular structure of a particular joint surface, and high density sampling methodologies (as proposed here) would be unwarranted. By homogenous, we do not mean to imply that trabecular parameters have the exact same value across the joint surface, but rather that values are randomly and uniformly distributed across the joint surface. If we can confidently reject the null hypothesis of homogeneity, we consider the alternative hypothesis that trabecular bone parameters are patterned, reflecting regions of higher and lower trabecular bone parameter values. We elect not to make functional hypotheses about the samples used in this study because, while the sample sizes are sufficient to demonstrate the method, they are not large enough to provide reliable statistical inferences about differences between the groups under examination.

2 | MATERIALS AND METHODS

2.1 | Sample and image acquisition

The proposed methodology is demonstrated here using two separate samples, one composed of tali from two genera of adult large-bodied apes, *Pan troglodytes* (female = 5, male = 0), *Pongo pygmaeus* (female = 2, male = 0), and *Pongo abelii* (female = 2, male = 0) and the other sample consists of modern human distal femora (female = 6, male = 4).

Computed tomography image stacks of the chimpanzee and orangutan tali were downloaded from MorphoSource (morphosource.org, Duke University, Boyer, Gunnell, Kaufman, & McGeary, in press) and details for these specimens can be found in Boyer and Seiffert (2013). These specimens were scanned on a GE eXplore Locus *in vivo* scanner at the Ohio University MicroCT Facility, and were reconstructed with isotropic voxel size of ~45 microns and saved as either 16-bit DICOM or TIFF image format. Additional scan parameters (i.e., acceleration voltage, tube current, filter) are not available for these scans. These specimens are parts of the collections curated by the American Museum of Natural History and the Smithsonian Institution National Museum of Natural History (Table 1).

The human distal femora are part of the William M. Bass Skeletal Collection curated by the Department of Anthropology at the University of Tennessee, Knoxville. All femora are from adult individuals that were between the ages of 21–55 years at the time of death and all are free of pathology. The distal femora were scanned on a BIR ACTIS 225/300 high-resolution μCT scanner at the Department of Human Evolution, Max Planck Institute for Evolutionary Anthropology. All specimens were scanned with an acceleration voltage of 130 kV, tube current of 100 μA and a 0.5-mm brass filter. Scans were reconstructed as either 2048 × 2048 or 3072 × 3072 pixel 16-bit TIFF images consisting of isotropic voxels, with edge dimensions of ~37 μm. Scans are curated by the Department of Anthropology at the University of Tennessee, Knoxville (Table 1).

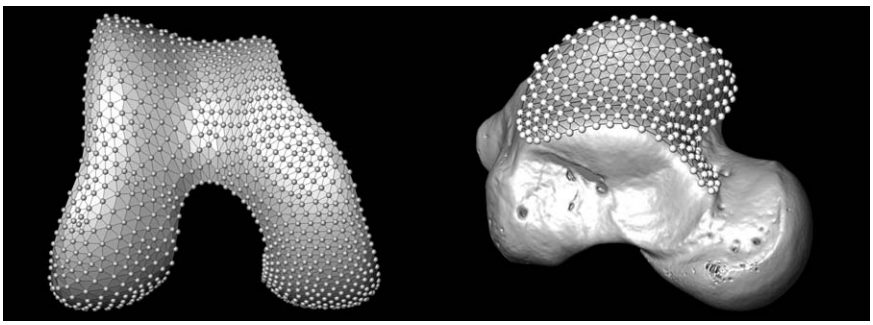

FIGURE 1 Sliding semilandmark configurations for the distal femur (left; 1007 landmarks) and talar trochlea (right; 201 landmarks)

2.2 | Image segmentation and surface model generation

Image segmentation is the process of partitioning a digital image into separate regions representing different areas/objects of interest. To segment the bone from the surrounding air we used the Optimise Threshold command for the BoneJ plugin for ImageJ (Doube et al., 2010; Schneider, Rasband, & Eliceiri, 2012) which optimizes the threshold value (Ridler and Calvard, 1978; Zhang, He, Fan, He, & Li, 2008) for a histogram of grayscale values to minimize connectivity density of the trabecular structure (Odgaard and Gundersen, 1993; Toriwaki and Yonekura, 2002). This process converts the 16-bit grayscale images (TIFF or DICOM) to binary images where white voxels represent bone and black voxels represent non-bone (i.e., air). Other segmentation processes have been suggested to produce more accurate results (Scherf and Tilgner, 2009); the goal of this research, however, was not to evaluate segmentation processes or provide particular trabecular bone parameter values for specific species, but rather was to demonstrate our geometric morphometric-based method for extracting VOIs. For tali, whole image stacks were processed using the Optimise Threshold algorithm. For the femora, because of the large size of the image stacks (>40 GB), three cubic VOIs (200 voxel edges) containing only trabecular bone were extracted from each femur, one in the middle of each condyle and one deep to the patellar surface. These cubic VOIs were processed using the Optimise Threshold command and the average of the three resulting threshold values was applied to the whole image stack. Surface models (PLY file format) of the external bone surface were generated in Avizo Lite 9.0.1 (FEI Visualization Sciences Group, 2015) following procedures outlined in Sylvester, Merkl, & Mahfouz (2008).

2.3 | Isolating trabecular bone from skeletal elements

For the tali, to separate the trabecular bone from the cortical bone shell, we followed the protocol advocated by Gross et al. (2014) and algorithms detailed in Pahr and Zysset (2009) which we implemented in MATLAB Version R2016a (MATLAB and Statistics Toolbox, 2016). Distinguishing between cortical and trabecular structure is necessary since, when placing a VOI inside a small and irregularly shaped skeletal element (such as the talus), it is possible that part of the VOI contains cortical bone from another region of the skeletal element. The process for separating cortical and trabecular structures (i.e., Gross et al., 2014; Pahr and Zysset, 2009) is briefly described here. The first step is to create an "outer mask" of the bone, which establishes the outer contour of the skeletal element. This outer mask is generated by carrying out a morphological closing (morphological dilation followed by morphological erosion using a spherical kernel) and opening (morphological erosion followed by morphological dilation) of the segmented image data, which serves to close small holes in the outer cortical shell of the skeletal element. The radius of the spherical kernel is approximately half the specimen's average trabecular thickness (Gross et al., 2014). Next, starting at the periphery of the outer bone mask, all voxels between the periphery of the outer bone mask and the first empty voxel (i.e., a trabecular space) along each of the primary voxel directions are detected. These detected voxels are then subtracted from the outer bone mask. The remaining image stack therefore approximates the voxels that represent the trabecular bone and trabecular space (collectively termed here the trabecular structure). A second morphological closing and morphological opening are then applied to this image stack to create a smooth cortical/trabecular boundary. We did not carry out separation of cortical bone from trabecular bone in the distal femur because the large size of the distal femur relative to the VOI radius. The placement of the VOIs in the distal femur was checked visually (detailed below) to ensure VOIs were completely immersed in the trabecular structure and any VOIs not completely contained within the trabecular structure were removed from the analysis for all specimens.

2.4 | Geometric morphometric analysis with sliding semilandmarks

As a first step in positioning the VOIs within the trabecular structure, we distributed sliding semilandmarks across the articular surface of each specimen using standard geometric morphometric techniques (Gunz and Mitteroecker, 2013; Sylvester, 2013). For each articular surface (i.e., the talar trochlea or distal articular surface of the femur), we first trimmed the articular surface from the rest of the surface model in Geomagic Wrap (3D Systems, 2015) using the "Trim by Curve" function. For both skeletal elements, the boundary of the subchondral articular surface is readily identifiable on the surface model. We did not include the regions of the talar trochlea, which accommodate articulations with the medial and lateral malleoli, by referencing the talar landmark configuration in Harcourt–Smith (2003). Next, a landmark

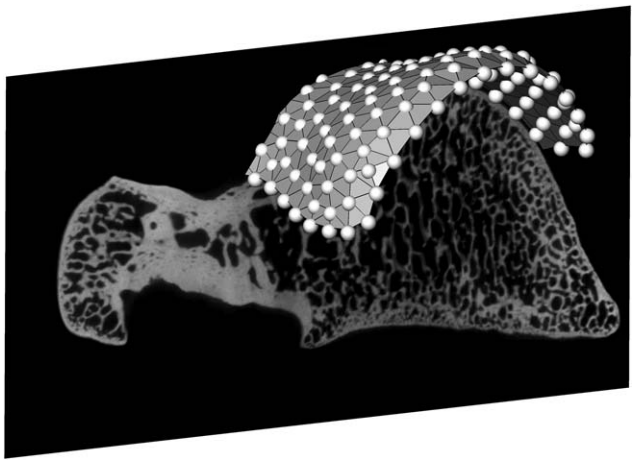

FIGURE 2 Sliding landmark configuration translated, rotated and scaled to the original position of the articular surface within the μCT image stack

template with the selected number of sliding semilandmarks (1007 for the femur; 201 for the talus) was created in Geomagic using one randomly selected specimen (Figure 1). The template was created by converting the surface model of the selected specimen to a point cloud, and then the point cloud was resampled to a uniform distribution of points. The number of points was selected to adequately capture the joint surface, which was evaluated by calculating the average distance between landmarks. For the tali, landmarks were approximately 1mm apart, while for the femora landmarks were approximately 2.5mm apart. We then used the "Wrap" function to convert the point cloud back to a triangulated surface model. This landmark template was then affine fit (including translation, rotation, scale, and shear) to all other specimens in the sample using the "Align Surface" module in Avizo Lite 9.1. Surface sliding landmarks from the template were projected onto the surface of each target specimen, and sliding landmarks along the trimmed edge were projected onto the corresponding trimmed edge of each target specimen.

Landmarks were then slid along tangent planes (surface landmarks) or tangent vectors (edge landmarks) to minimize the bending energy of the thin-plate spline interpolation function relative to the updated Procrustes average (Gunz and Mitteroecker, 2013). During the sliding process, landmarks slid off the anatomical structure (Gunz and Mitteroecker, 2013), and so landmarks were projected back onto the surface model. After sliding (i.e., when the landmarks reached stable positions), all landmark configurations were aligned using Generalized Procrustes Analysis (GPA), which removes information about size, location and orientation. Procrustes coordinates were then used to calculate a Procrustes average specimen, which was used as the reference configuration for the next round of sliding. This two-step process (sliding/projecting until stable landmark positions were reached, followed by a GPA) was repeated until the Procrustes average configuration became stable.

Finally, sliding landmark configurations were returned to their original size by multiplying the coordinates of a specimen by the centroid size of that specimen, and returned to their original location and orientation (i.e., configurations were realigned with the CT image stack coordinates) (Figure 2). This was accomplished using the "Align Surface" module in Avizo Lite 9.1 to fit the landmark configuration surface to the original surface model.

2.5 | Positioning the VOI

We extracted a single spherical VOI for each sliding landmark based on the position of that sliding landmark and its associated surface normal vector (i.e., a unit vector perpendicular to the surface model at that landmark position), and the depth of the trabecular structure. The center of a particular VOI was constrained to lie along the surface normal, which originates from its associated sliding landmark (Figure 3a). We positioned the VOIs immediately deep to the cortical shell of the articular surface following the logic that transarticular forces accommodated by the trabecular structure must past through the trabeculae closest to the load-bearing surface. Analyzing this portion of the trabecular structure maximizes the probability of finding patterns in the trabecular structure that reflect loading history and behavioral repertoire. We do not mean to argue that deeper portions of the trabecular structure do not carry functional signals. Instead, we suggest that trabeculae immediately deep to a particular portion of the cortical shell are likely to be a more direct and proximate part of the load transfer path, transferring load to deeper portions of the trabecular structure. In contrast, deeper portions of the trabecular structure likely accommodate a variety of loads from larger regions of the joint surface, as they transfer loads from the epiphyses to the diaphysis. This parallels the logic used by Carlson and Patel (2006), Polk, Blumenfeld, & Ahluwalia (2008), Patel and Carlson (2008), and Nowak, Carlson, & Patel (2010), who examined apparent density in subchondral bone. The radius of the VOI was determined based on recommendations in Gross et al. (2014) and scaled for each specimen (Ryan and Shaw, 2012) based on centroid size. For tali, VOIs varied from 3 mm for the smallest specimen to 4 mm for the largest, while for femora VOIs ranged from 3.7 mm to 5 mm.

The greatest challenge for positioning the VOI was determining the depth from the outer surface of the skeletal element. We determined the depth at which to place the VOI using information about the position of the trabecular structure (trabecular bone and/or space). In the case of the tali, one result of separating the cortical and trabecular bone, as described above, was an image stack in which the total trabecular structure (trabecular bone and trabecular space) is represented by white voxels and all other voxels are black; thus the local thickness of the cortical shell is knowable. In the case of the femora, we created an outer bone mask using the procedure described by Pahr and Zysset (2009). These data, combined with the original segmented image stack, allowed us to identify those voxels that represented trabecular space (Figure 4a–d).

Calculating the position of the VOIs begins by calculating the coordinate position (XYZ Cartesian coordinate position) of each of the voxels representing the trabecular structure (or space). Next, the coordinate positions of the trabecular structure voxels are projected onto the normal vector of the current sliding landmark. The Euclidean

distance from each trabecular structure voxel to its projected position on the normal vector is calculated, and any voxel with a Euclidean distance that is larger than the radius of the VOI is discarded from further consideration. This extracts a cylinder of trabecular structure voxels in which the central axis of the cylinder is the surface normal, and the radius of the cylinder is equal to the radius of the VOI (Figure 3b). Then, using the remaining trabecular structure voxels (i.e., the cylinder of retained voxels), we calculate the position of a "positioning sphere" (i.e., a sphere with the same radius as the VOI). The position of this sphere is the point at which it would first encounter a trabecular structure voxel if it were sliding down the surface normal vector deeper into the skeletal element from outside the skeletal element (Figure 3c). Then the position of the VOI is calculated such that its center is along the surface normal vector, and its surface is touching (and deep to) the surface of the positioning sphere. A cube of voxel data large enough to include the VOI is extracted and all voxels outside the spherical VOI (i.e., voxels with a Euclidean distance from the VOI center greater than the VOI radius) are turned black.

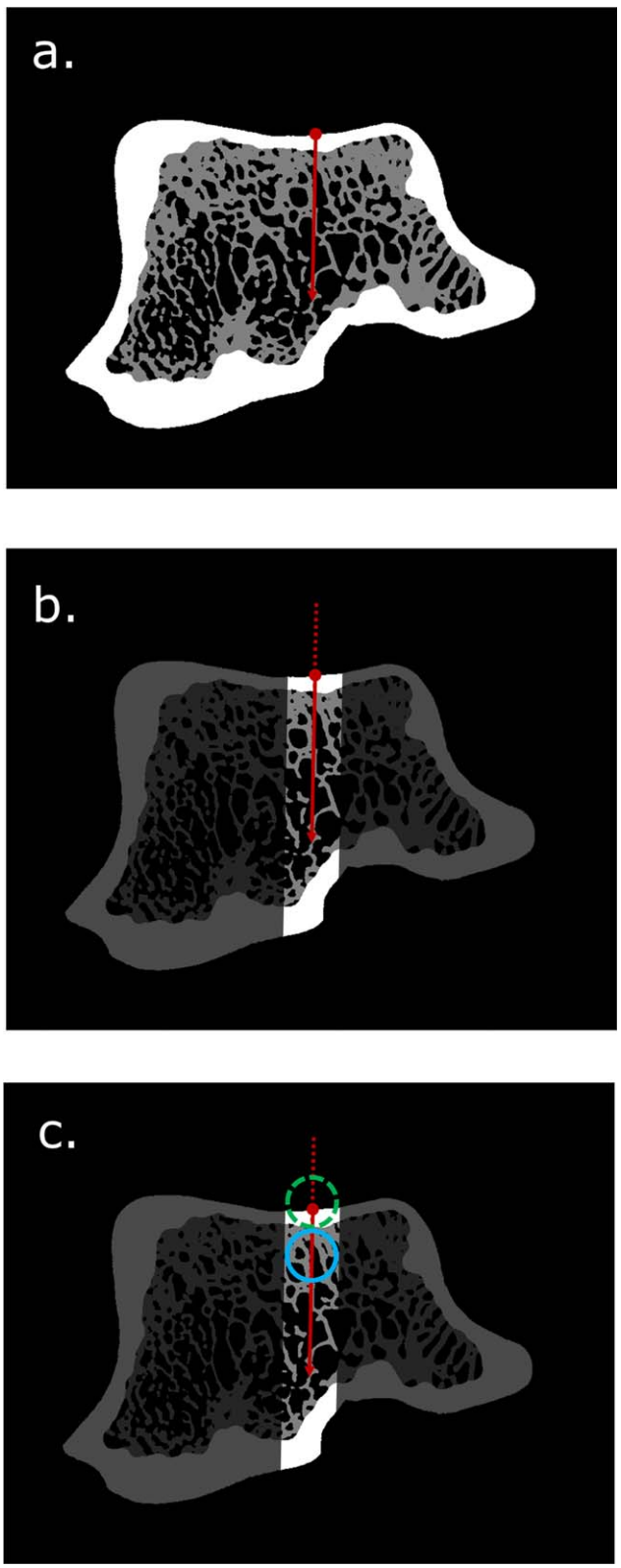

FIGURE 3 Depiction of VOI positioning algorithm. For ease of interpretation this is a 2D representation of the 3D process. All vectors should be considered 3D vectors and circles are used to represent spheres. (a) Cortical shell (white) and trabecular bone (grey) with single sliding semilandmark (red dot) and associated surface normal (red arrow). (b) Trabecular bone cylinder retained for further consideration (normal) and trabecular bone eliminated from further consideration (shadowed). (c) Positioning sphere (green circle) placed such that the center of the sphere is along the vector of the surface normal and its deepest surface is tangent to the most superficial voxel representing the trabecular structure; VOI (blue circle) placed deep to the positing sphere with its center constrained to be equal to the surface normal vector

2.6 | VOI quality

For small complex skeletal elements such as the talus, positioning VOIs using the above procedure may result in some VOIs that also include cortical bone and/or voxels outside the skeletal element. This can occur in places where the skeletal element is thinner (in the direction of the surface normal) than the VOI (Figure 5). Including non-trabecular structure in the analysis can alter the values of calculated trabecular bone parameters and thus should be avoided. We calculated the number of non-trabecular structure voxels included in each VOI by extracting the same VOIs (position and radius) from an image stack in which non-trabecular structure voxels (i.e., cortical bone and air outside the skeletal element) are white and the trabecular structure is black (i.e., the image voxel values have been inverted). This allowed us to calculate the percentage of each VOI that was within, and outside, the trabecular structure.

To determine how much of the VOI could be outside the trabecular structure and still obtain reliable trabecular bone parameters, we ran a series of simulations. To do this, we examined 90 VOIs (10 from each of the 9 tali) that contained more than 99.9% trabecular structure. For these 90 VOIs we calculated four standard trabecular bone parameters: bone volume fraction (BV/TV), trabecular thickness (Tb.Th), trabecular spacing (Tb.Sp), and degree of anisotropy (DA). Then, iterating sequentially through the VOI image stack slice-by-slice, we changed all white bone voxels, up to the current image slice, to black air voxels, and then recalculated the trabecular bone parameters. For example, in the third

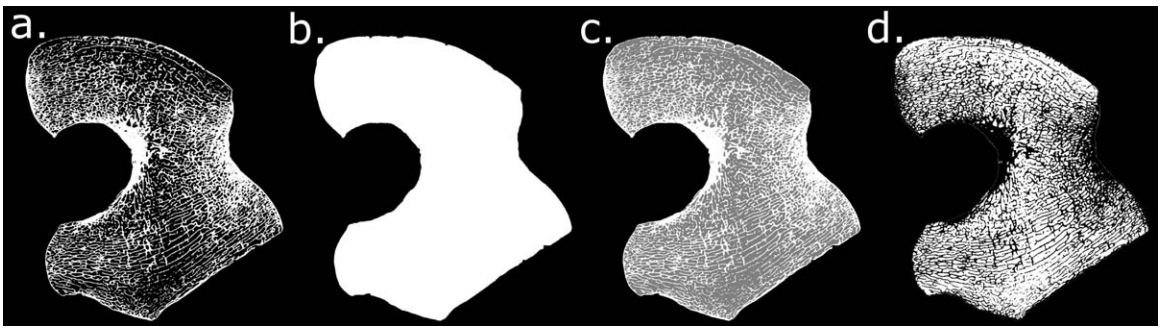

FIGURE 4 These images show the method for isolating the trabecular space from the original segmented image stack. (a) Original segmented image stack. (b) Outer mask formed by closing boundary of segmented image stack and filling the image. (c) Average of images in (a) and (b) (white = 1, black = 0, when pixel values for images a and b are averaged trabecular space voxels equal 0.5). (d) Image showing all the identified trabecular space voxels (i.e., those voxels in image c with a value of 0.5)

iteration, the first three image slices containing bone (white) voxels were turned completely black, thus simulating the scenario in which these slices represented cortical bone that had been removed. In practice this resulted in removing ~0.1–1.5% of the trabecular structure with each iteration. Trabecular thickness and spacing are reported as the percent absolute change from the original value, while bone volume fraction is reported as an absolute change from the original value. Because DA is calculated based on random vectors projected through a VOI (Doube et al., 2010), the value of this parameter can fluctuate with repeated measures of the same VOI. Consequently we measured DA on the complete, unaltered VOI five times before beginning the partial VOI simulation. We provide the full details of the results of our simulation in the Results section below, but in general we found that trabecular parameters were acceptable if at least 90% of the VOI was embedded in the trabecular structure.

For the femoral analysis, ensuring that no proportion of any VOI was outside of the trabecular structure was easier because of the large size of the bone relative to the VOI. To check this, we visualized all 1007 VOIs overlaid upon each image stack. To do this we created a "Landmark Set" in Avizo Lite 9.1, in which each VOI was visualized by a spherical landmark. The landmarks were then scaled to the size (i.e., diameter) of the VOIs for that specimen. All femora were inspected to insure that all VOIs were completely contained within the trabecular structure by scrolling through the image stack and comparing the cortical/trabecular boundary relative to the superficial surface of the VOIs. It was determined that the VOIs associated with landmarks along the boundary of the articular surface frequently projected outside of the skeletal element and/or incorporated cortical bone. Consequently these 141 VOIs were discarded, leaving 866 VOIs for further analyses.

2.7 | Trabecular bone parameters

We quantified trabecular thickness (Tb.Th) and trabecular spacing (Tb.Sp) in BoneJ using the "Thickness" function prior to extracting the VOIs. We did this because trabeculae that lie on the boundary of a spherical VOI will have portions outside the VOI "sliced off" when the VOI is extracted. As a result, if thickness values were calculated after the VOIs were extracted, values could be lowered artificially. To calculate Tb.Th, we applied the "Thickness" function directly to the full segmented image stack. For Tb.Sp we created an image stack in which trabecular space was represented by white voxels and all other voxels were black and then applied the "Thickness" function to this image stack. The BoneJ function outputs a new image stack which is a copy of the original image stack in terms of structure, the difference is that instead of the image stack being binary (white = bone, black = air) the value of the voxels representing bone are the local thickness value (Doube et al., 2010). Volumes of interest were then extracted from the thickness image stacks and mean trabecular thickness and spacing for each VOI were calculated. BV/TV and DA were calculated in BoneJ from VOIs extracted from the original segmented image stack (binary data). Extracted VOIs were batch processed in BoneJ by writing a macro for ImageJ to process each VOI sequentially. Bone volume fraction values for the tali were adjusted to compensate for portions of the VOI outside the trabecular structure (i.e., the denominator of BV/TV was adjusted based on calculated VOI quality as described above). It is important to note that because the image stacks representing trabecular thickness and spacing represent the exact same bone structure as the original binary image stack, any particular VOI is quantifying the exact same portion of the trabecular structure independent of which image stack is currently being examined or variable being calculated.

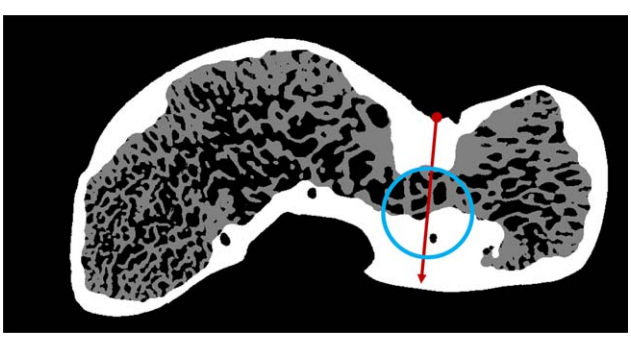

FIGURE 5 Example of a situation where a VOI may include cortical bone and should be eliminated from further consideration and analyses. Symbols are as explained in Figure 3. For ease of interpretation this is a 2D representation of the 3D process. The vector should be considered a 3D vector and the circle represents a sphere

2.8 | Statistical analysis

To test the hypothesis that trabecular parameters are homogeneous across joint surfaces, we used Moran's I (Cliff and Ord, 1981) which is a measure of spatial autocorrelation. It tests if values for a variable of interest are clustered, dispersed, or randomly distributed across spatial locations. The index can vary between negative one and one, where negative one indicates perfect dispersion, one indicates clustering of similar values, and zero indicates a random distribution. The index requires the researcher to create a weights matrix that quantifies the spatial relationship between value locations. Common approaches to the weights matrix include: giving neighbors a weight of one and others a weight of zero; the inverse of the distance between locations; and the inverse of the squared distance between locations (Getis and Aldstadt, 2002). We employed all three of the weighting approaches using connectivity of the mesh surface to define neighbors (neighbors share an edge), and the distance of the Dijkstra's path (Dijkstra, 1959) for distance based weights. Closed form solutions as well as randomization procedures can be used to generate *p* values for Moran's I (Anselin, Syabri, & Kho, 2006; Cliff and Ord, 1981). We conducted both, although we present only the latter because there was no difference in test results. The randomization procedure involves randomly assigning variable values to locations and recalculating the Moran's I value (9,999 iterations). We calculated Moran's I values for the average chimpanzee talus, average orangutan talus, and average human distal femur for all four trabecular bone values investigated.

A significant strength of the geometric morphometric toolkit is the ability to visualize mean shapes and to compare mean shapes for groups of interest. Because the described procedure uses the homology of sliding landmarks to position the VOIs, the resulting trabecular parameters calculated for each VOI can be statistically compared between groups, and group means can be calculated for each VOI and mapped onto surface models. Here we compared *Pan* vs. *Pongo* tali and human female vs. human male distal femora. Our intent was not to make statements about behavioral differences between these groups or functional interpretations, only to demonstrate how such comparisons can be made. First, we wanted to know if the groups of interest differed in their patterns of trabecular bone parameter distribution (i.e., which areas of the skeletal element have relatively high and low trabecular bone parameter values) without regard to the magnitude of the particular trabecular bone parameter values. Second, we wanted to include information about the magnitude of the trabecular bone parameters in analyzing the pattern of distribution. We consider this parallel to the practice of analyzing shape space and form space in GM analyses (Mitteroecker, Gunz, Bernhard, Schaefer, & Bookstein, 2004). To compare patterns of trabecular bone, we converted each specimen's values for a particular trabecular bone parameter into *z*-scores based on that specimen's mean and standard deviation of all VOIs. To examine patterns of trabecular bone distribution with magnitude, we analyzed the original data values.

We tested for differences between groups using a nonparametric permutation/randomization-based version of the MANOVA test which is specifically designed for dealing with 'high-dimensional data' (i.e., samples in which the number of variables exceeds the number of observations) (Collyer, Sekora, & Adams, 2015). The traditional

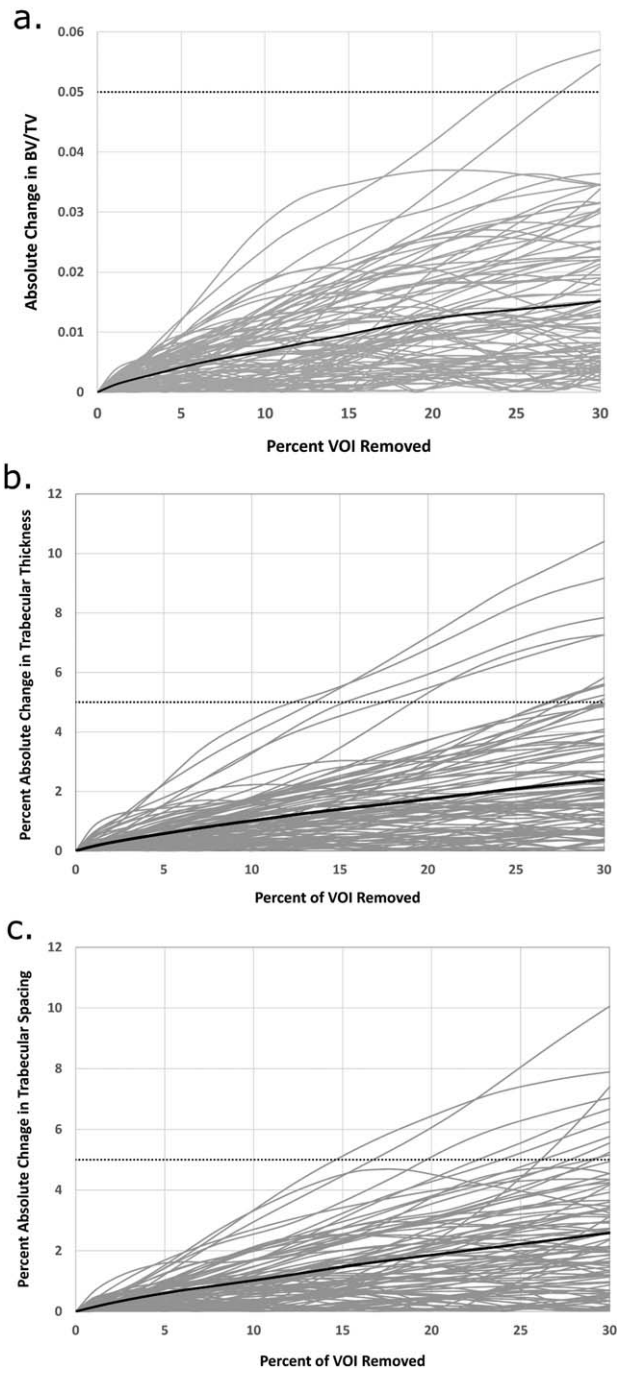

FIGURE 6 Results of VOI quality simulation analyses. (a) Absolute change in bone volume fraction (BV/TV; *y* axis) plotted against percent of VOI (and trabecular bone) removed (*x* axis). (b) Percent absolute change in trabecular thickness (Tb.Th) as a function of VOI removed. (c) Percent absolute change in trabecular spacing (Tb.Sp). For each panel, each grey line represents one of the 90 VOIs analyzed; the solid black line represents the average of the 90 separate VOIs; dotted line represents 5% change level

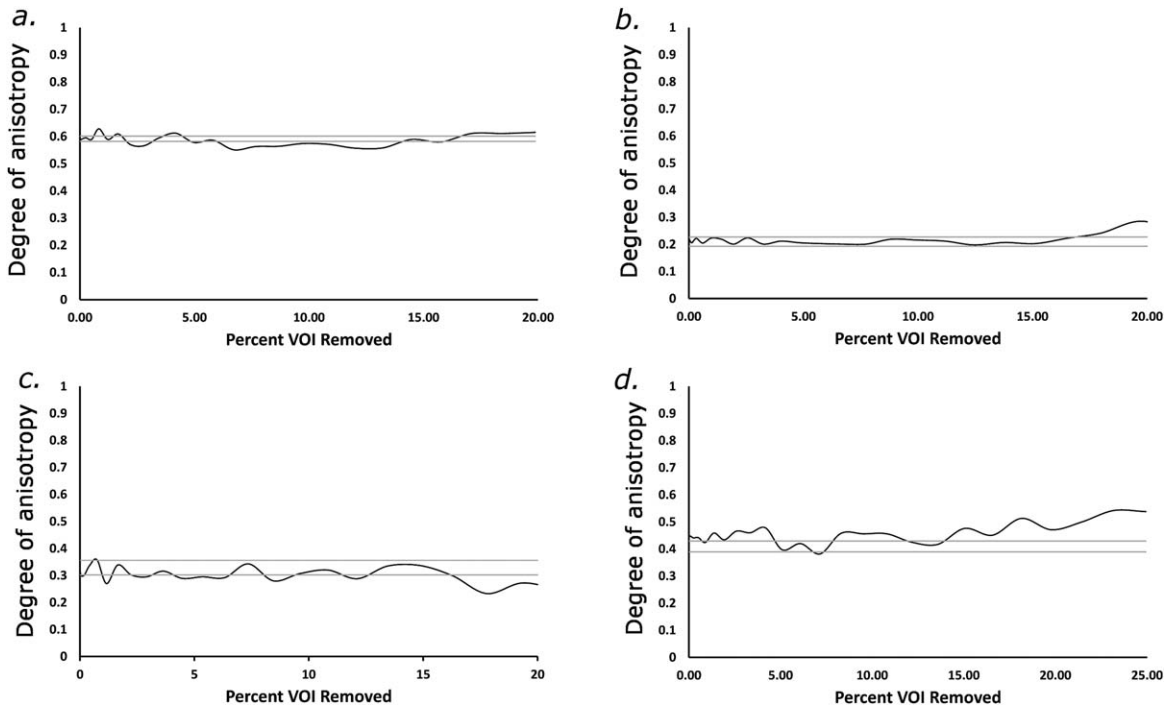

FIGURE 7 Examples of change in degree of anisotropy (DA) plotted against percent of VOI removed. Grey lines represent variation (max vs. min value) in DA value from repeated ($n = 5$) measurements of DA on the full VOI trabecular structure. Black line represents change in DA as a function of percent VOI removed

multivariate test for comparing two groups for several dependent variables is a (parametric) MANOVA; however, such a test would not be appropriate given the nature of these data. The extracted VOIs overlap to varying degrees because of their size and high density across the joint surface. Consequently, trabecular bone parameters from closely spaced VOIs are likely to be highly correlated (i.e., the problem of multicollinearity). Also, the parametric MANOVA relies on the number of observations being larger than the number of variables, and when the latter exceeds the former the test cannot be performed (Collyer et al., 2015). VOIs could be removed from the analysis to create a smaller number of non-overlapping VOIs, however because the trabecular structure is continuous it is not clear this would resolve this problem and potentially interesting information (the distribution of trabecular bone) would be lost. As advocated, and detailed, by Collyer et al. (2015), we used the residual randomization permutation procedure for generating an F-distribution as described by Anderson and Robinson (2001) and Freedman and Lane (1983). This test considers two general linear models to explain the dependent variables: 'the null model' which includes only the intercept term, and the "full model" which includes an independent (dummy) variable representing group membership. The test *F*-value is calculated as the difference between the sum of squares of the "full" and "null" models, divided by the sum of squares of the "null model" each adjusted for the appropriate degrees of freedom. For a case with a single independent variable, the F-distribution is generated by randomly permuting the dependent variables among cases (observations) and recalculating the *F* value based on a new "full model." The *P* value is calculated by comparing the test *F* value to the generated *F* distribution. We accepted statistical significance at the 0.05 level. Significant tests were followed up by creating color maps which depict group mean values for the relevant trabecular bone parameter. We also carried out principal component analyses (PCA) of variables with significant *p*-values in order to visualize separation between groups; this allowed us to identify individual specimens representing extremes of the trabecular bone patterns for additional visual comparison. Finally, we used Gaussian mixture modeling to compare distributions of group-specific average trabecular bone parameters and evaluated competing models using the Akaike information criterion (AIC) and the Bayesian information criterion (BIC).

3 | RESULTS

3.1 | VOI quality for talus analysis

The simulation analyses suggest that as much as 10% of the VOI may be outside of the trabecular structure and still produce stable trabecular bone properties. For the 90 VOIs examined, the average of absolute change in BV/TV values was <0.7% (Figure 6a). The maximum change in BV/TV with a 10% reduction in VOI was <3%, and 88 of the 90 VOIs changed by <2%. Trabecular thickness and spacing values were considered stable when 10% or less of the VOI was removed, as both parameters changed by <5% of their original values and in most cases by <3% (Figure 6b,c). Most DA values were not heavily affected by removal of 10% or less of the trabecular bone structure contained within the VOI. Figures 7a–d shows four extreme examples, two in

TABLE 2 Moran's I spatial autocorrelation

Genus	Variable	Weights matrix	Moran's I
Homo	BV/TV	Binary	**0.88**
		Inverse distance	**0.23**
		Inverse squared distance	**0.57**
	Tb.Th	Binary	**0.76**
		Inverse distance	**0.22**
		Inverse squared distance	**0.47**
	Tb.Sp	Binary	**0.86**
		Inverse distance	**0.21**
		Inverse squared distance	**0.55**
	DA	Binary	**0.93**
		Inverse distance	**0.32**
		Inverse squared distance	**0.60**
Pan	BV/TV	Binary	**0.64**
		Inverse distance	**0.12**
		Inverse squared distance	**0.33**
	Tb.Th	Binary	**0.60**
		Inverse distance	**0.16**
		Inverse squared distance	**0.36**
	Tb.Sp	Binary	**0.56**
		Inverse distance	**0.12**
		Inverse squared distance	**0.31**
	DA	Binary	**0.64**
		Inverse distance	**0.12**
		Inverse squared distance	**0.33**
Pongo	BV/TV	Binary	**0.55**
		Inverse distance	**0.12**
		Inverse squared distance	**0.30**
	Tb.Th	Binary	**0.75**
		Inverse distance	**0.19**
		Inverse squared distance	**0.45**
	Tb.Sp	Binary	**0.59**
		Inverse distance	**0.13**
		Inverse squared distance	**0.34**
	DA	Binary	**0.55**
		Inverse distance	**0.12**
		Inverse squared distance	**0.30**

Bold Moran's *I* values significant at the 0.0001 level.

which DA stays well within the boundaries of the five repeated measurements of DA on the whole VOI, and two in which DA varies greatly. Thus for all subsequent analyses of the talus, we retained only those

TABLE 3 Nonparametric permutation MANOVA results for ape tali

Pan vs *Pongo* trabecular bone properties	
Property	***P* value**
BV/TV	0.432
BV/TV *z*-score	0.078
Tb.Th	0.757
Tb.Th *z*-score	0.115
Tb.Sp	0.271
Tb.Sp *z*-score	**0.036**
DA	**0.003**
DA *z*-score	**0.020**

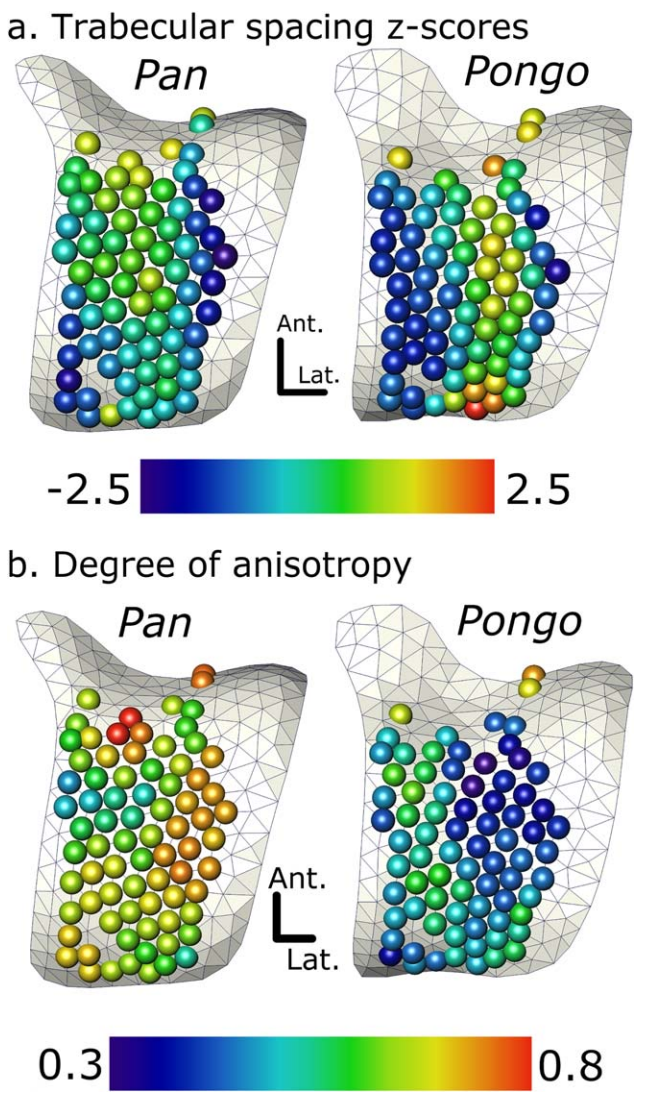

FIGURE 8 Color map of (a) trabecular spacing (Tb.Sp) *z*-scores and (b) DA for chimpanzee (left) and orangutan (right) talar trochlea overlaid on average shapes for each species. Tb.Sp *z* score values range from −2.5 (purple; i.e., relatively smaller spaces between trabeculae) to 2.5 (red; i.e., relatively larger spaces between trabeculae). DA values range from 0.3 (purple; i.e., trabeculae are more isotropic) to 0.8 (red; i.e., trabeculae are more anisotropic)

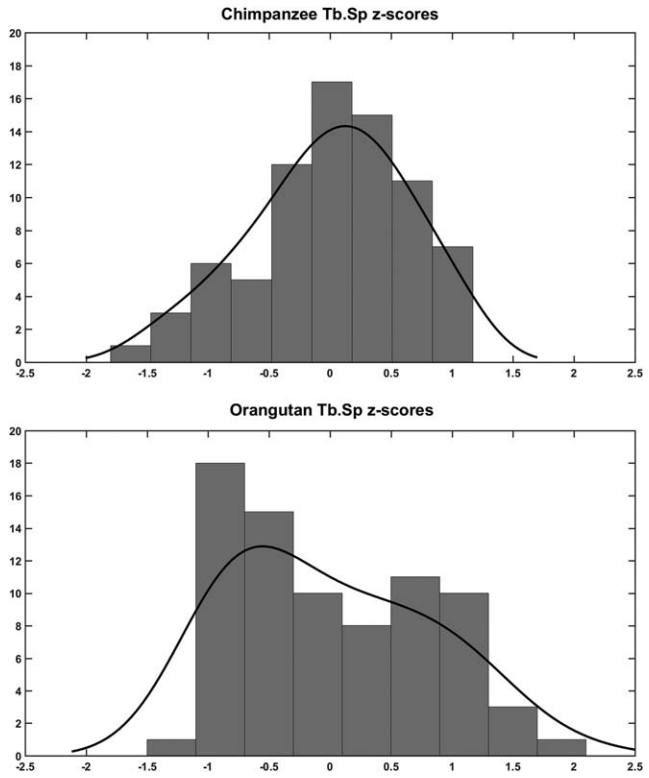

FIGURE 9 Histograms of average trabecular spacing (T.Sp) *z*-scores for chimpanzee (top) and orangutan (bottom) with kernel distribution overlay (black lines). The orangutan sample demonstrates a bimodal distribution, a finding supported by Gaussian mixture model analysis, while the chimpanzee sample shows a unimodal distribution

VOIs that included more than 90% trabecular structure. This exclusion criterion required that we remove 124 of the original 201 VOIs sampled, leaving 77 VOIs for analysis.

3.2 | Test for trabecular bone spatial homogeneity

Results from the spatial autocorrelation analysis (Moran's *I*) are provided in Table 2. In all 36 cases the Moran's *I* value was positive and significant ($p < 0.0001$), indicating that trabecular bone parameter values are clustered across the joint surfaces investigated here (i.e., they are not homogeneously distributed). For all variables investigated, using the binary weights matrix (1 = neighbors, 0 = non-neighbors), produced the highest Moran's *I* values, while using the inverse of the distance between VOI locations produced the lowest Moran's *I* values.

3.3 | Great ape tali

Results from nonparametric permutation MANOVA tests comparing tali of *Pan* and *Pongo* are provided in Table 3. These tests did not reveal a statistically significant difference between the two apes for raw values of BV/TV, Tb.Th and Tb.Sp values or *z*-scores of BV/TV and Tb.Th. The chimpanzee and orangutan tali were found, however, to be statistically different when compared for Tb.Sp *z*-scores ($p = 0.036$). Species-specific average color maps for this parameter are provided in Figure 8a and show that spacing is more uniform across the joint surface of *Pan* relative to *Pongo*. On average, orangutans exhibit a region of relatively high trabecular spacing along the lateral portion of the articular surface and relatively low trabecular spacing along the more medial portion of the articular surface whereas spacing is more uniform in the chimpanzee talus. This assessment of the color maps is reinforced by examining the distribution of species-specific average Tb.Sp *z*-scores which shows the chimpanzee to be unimodal and the orangutan to be bimodal (Figure 9). The results of the Gaussian mixture models support this (Table 4); the distribution of Tb.Sp *z*-scores for the average chimpanzee had the lowest AIC and BIC for a single component model, while both criterion values are lowest for the two component model for the orangutan data.

Chimpanzees and orangutans were also significantly different for DA ($p = 0.003$) and DA *z*-scores ($p = 0.020$) indicating that both the magnitude and pattern of DA were different between the groups. Figure 8b shows color maps of average DA for both *Pan* and *Pongo*, and Figure 10 shows a plot of the first two principal components based on DA values (PC1 represents 63.7% of the sample variance, and PC2 represents 17%). The PC coefficients (i.e., values of the eigenvector) associated with PC1 were all positive, hence a more positive PC score indicates greater DA values for all VOIs. In other words, as specimens increase in value along PC1, DA values for all VOIs are increasing. In general, the *Pan* specimens have much higher PC1 scores indicating that the trabecular structure in the chimpanzee talus is more anisotropic, while the trabecular structure of the orangutan talus is more isotropic.

3.4 | Human distal femora

The nonparametric permutation MANOVA tests did not reveal statistically significant differences between male and female distal femora for most trabecular bone parameters. *p*-values were greater than the selected alpha value ($\alpha = 0.05$) for all tests except that comparing the *z*-scores of Tb.Sp ($p = 0.037$, Table 5). A plot of the first two principal components based on Tb.Sp *z*-scores is provided in Figure 11 and demonstrates a general separation between males and females. The difference between the sexes appears to be driven, at least in part, by two males with high positive PC1 scores. For comparison, Tb.Sp *z*-scores color maps for the two individuals at the extreme positive and negative ends of PC1 (one female and one male) are provided in Figure 12 along with color maps of the average male and female patterns. These images demonstrate that the females in the sample have a region of relatively high trabecular spacing along the medial edge of the medial condyle,

TABLE 4 Gaussian mixture model *Pan* and *Pongo* Tb.Sp *z*-scores

Component number	*Pan*		*Pongo*	
	AIC	BIC	AIC	BIC
1	**153.2**	**157.8**	190.3	195.0
2	155.8	167.6	**177.0**	**188.7**
3	156.8	175.5	180.4	199.2

Bold values indicate lowest value for each species and criterion.

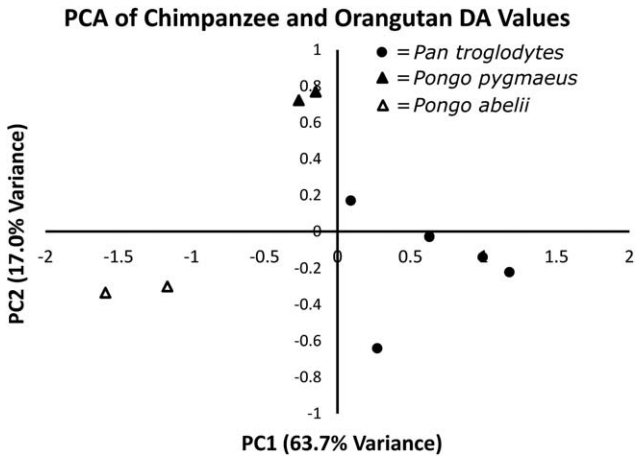

FIGURE 10 Plot of first two principal components of degree of anisotropy (DA) values for chimpanzees and orangutans

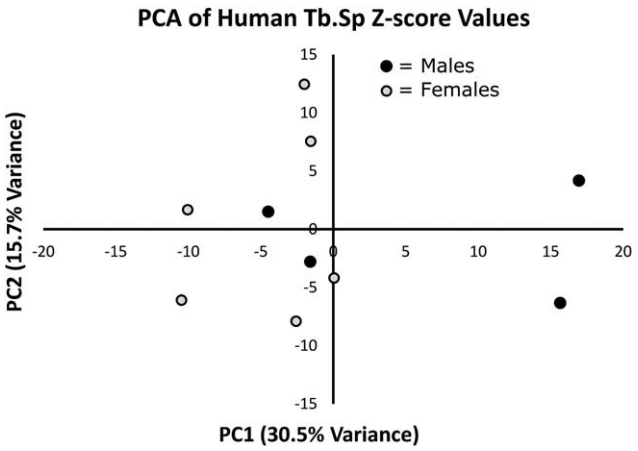

FIGURE 11 Plot of first two principal components of trabecular spacing (Tb.Sp) z-scores for modern humans

while males have more uniform trabecular spacing. This pattern can also be appreciated in slices through the medial condyles of these two specimens (Figure 13). Average human BV/TV, Tb.Th, Tb.Sp and DA color maps are provided in Figure 14.

4 | DISCUSSION

4.1 | VOI sampling procedure

The results presented here allow us to reject our null hypothesis that trabecular bone parameter values are homogenous across the joint surfaces. This result is similar to the work of other researchers who have sampled multiple VOIs and found that trabecular bone parameter values vary across joint surfaces (Chirchir et al., 2017; Griffin et al., 2010). This suggests that single VOI analyses of trabecular structures are likely to miss valuable trabecular bone patterns which may reveal important functional information. All spatial autocorrelation analyses demonstrated that trabecular bone parameter values are clustered, exhibiting regions of relatively high and low values. Further, the patterns of trabecular bone present in these joint surfaces suggest that using several VOIs would only work if the VOIs were placed strategically to capture variation. These critical VOI positions, however, cannot be known beforehand and thus argue for dense VOI sampling techniques such as the method presented here.

The presented analyses demonstrate that our procedure can quantify variation in trabecular bone parameters across joint surfaces, demonstrating group-level (e.g., species, sex) differences in both talar and femoral trabecular structure. Importantly, this method promises the

TABLE 5 Nonparametric permutation MANOVA results for human femora

Female vs. male trabecular bone properties	
Property	***P*-value**
BV/TV	0.357
BV/TV *z*-score	0.110
Tb.Th	0.105
Tb.Th *z*-score	0.187
Tb.Sp	0.425
Tb.Sp *z*-score	**0.037**
DA	0.201
DA *z*-score	0.074

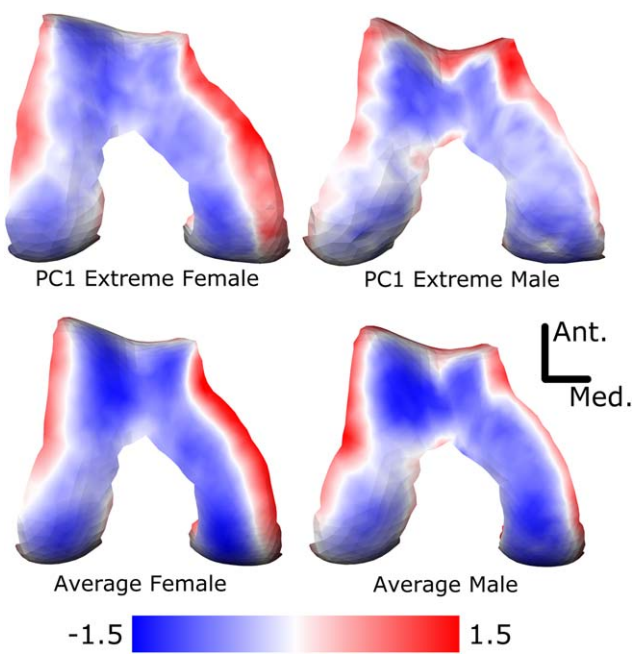

FIGURE 12 Color maps of trabecular spacing (Tb.Sp) z-scores. Red = positive z-score, i.e. relatively larger spacing; Blue = negative z-score, i.e. relatively smaller spacing; White = 0. Top row: female (left) and male (right) at the extremes of the first principal component scores for this variable. Bottom: female (left) and male (right) average shapes with average Tb.Sp z-scores values

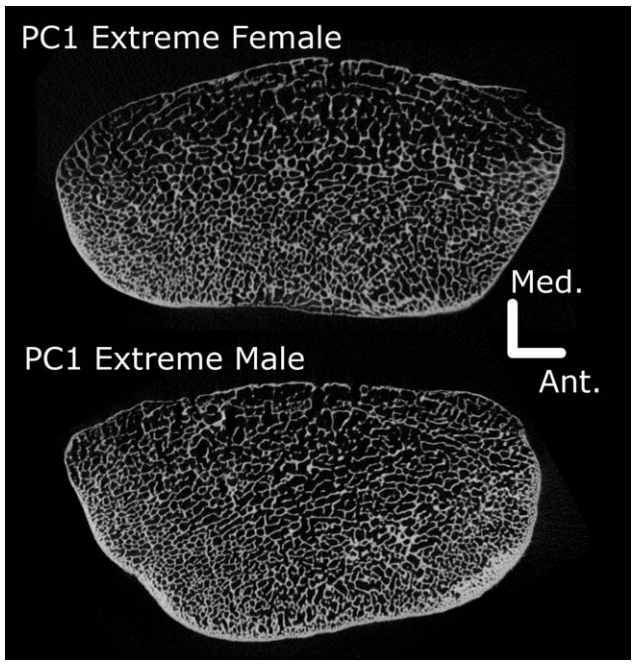

FIGURE 13 Transverse slices through the medial condyles of the female and male humans that are at the extremes of PC1 from the principal components analysis of the trabecular spacing (Tb.Sp) *z*-scores (specimens correspond to those depicted in the top two panels of Figure 12)

potential to reveal behavioral signals contained within trabecular structure across a range of anatomical structures and taxa. Fundamentally, our approach mirrors the work of Carlson and Patel (2006), Polk et al. (2008), Patel and Carlson (2008), and Nowak et al. (2010), who examined apparent density in subchondral bone. In these articles, voxel gray-scale values are equated with apparent density, and the researchers examine the distribution of apparent density of the voxels representing trabecular bone. The logic of the approach of sampling near the articular surface is sound; if a force is applied normal to a particular portion of the joint surface, the load transfer path will travel through the underlying trabeculae (Gefen and Seliktar, 2004; Zhou et al., 2014). This approach therefore maximizes the probability of sampling trabeculae that may reveal a behavioral signal.

Gross et al. (2014) successfully demonstrated variation in trabecular structure across a skeletal element, but, as they acknowledge, their procedure does not allow for statistical comparison between groups (Kivell, 2016). To our knowledge, our procedure is the first to sample the trabecular structure continuously across large portions of joint surfaces, and which also allows for making statistical comparisons between groups. The basis for our methodology, sliding semilandmarks, is a technique that is becoming increasingly common in geometric morphometric analyses, because of its flexibility and ability to locate (geometrically, if not biologically) homologous positions on biological structures. This approach combined with techniques for separating trabecular bone (and space) from cortical bone (Pahr and Zysset, 2009; Gross et al., 2014) provide sufficient information to place VOIs in the trabecular structure immediately deep to the subchondral bone/cortical shell.

Because the VOIs are placed automatically, it is likely that some VOIs may not be contained entirely within the trabecular structure, and this seems especially true for smaller bones. A strength of this technique is that it allows the percent of VOI outside the trabecular structure to be quantified (VOI quality) and/or VOI positions to be visualized, so that unreliable VOIs can be discarded from further analyses. Results of our simulations of removing portions of the trabecular structure suggest that as much as 10% of a VOI may lay outside the trabecular structure and still provide reliable BV/TV, Tb.Th, Tb.Sp, and DA values. In our analysis of the tali, we calculated the percent of the VOI outside the trabecular structure and used this to adjust the total volume (TV) values in calculating BV/TV. For the femora, visualizing the VOIs allowed us to identify VOIs outside the trabecular structure and all such VOIs were discarded from the analysis, obviating the need to adjust VOI total volume values. We encourage researchers that intend to employ this technique to carry out simulations of their own samples to see the effect of including partial VOIs in the analysis.

4.2 | Chimpanzee and orangutan tali

Our analysis was able to distinguish between chimpanzee and orangutan tali based on variation in DA across the joint surface as well as the pattern of trabecular bone spacing. In general, the chimpanzee talus has higher DA values, indicating that the trabecular structure is more highly oriented across the trochlea of the chimpanzee talus compared to that of orangutans. In their analysis of talar trabecular structure, DeSilva and Devlin (2012) also found chimpanzees to have higher DA values, although this statistically significant result was only present in

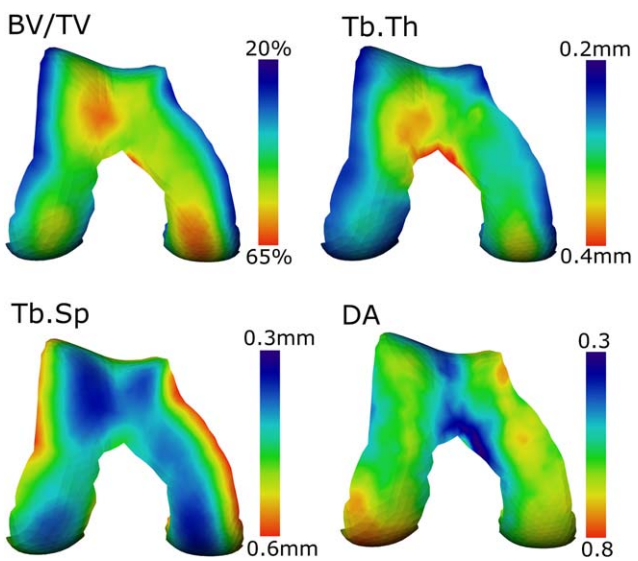

FIGURE 14 Color map of average human distal femur showing distributions of trabecular bone parameters. Cooler colors are lower values and warmer colors are higher values. Values included after each parameter represent the low (purple) and high (red) values. Bone volume fraction (BV/TV; top left; 20–65%); trabecular thickness (Tb.Th; top right; 0.2–0.4 mm); trabecular spacing (Tb.Sp; lower left; 0.3–0.65 mm); and degree of anisotropy (DA; lower right: 0.3–0.8)

the posterolateral quadrant of the talus. In addition, the Tb.Sp was more homogeneous across the chimpanzee joint surface, while the orangutan talus showed areas of relatively low and high trabecular spacing. In contrast, DeSilva and Devlin (2012) found chimpanzees to have more variable Tb.Sp values, and orangutans to have more homogenous spacing.

Although our goal was not to make statements about functional differences between these two species (and any conclusions should be considered speculative and tempered by the small samples examined here), differences between the species for both trabecular parameters are generally consistent with the documented locomotor repertoires of each species. Chimpanzees utilize significant amounts of terrestrial quadrupedalism (Doran, 1996; Doran and Hunt, 1994), a form of locomotion which may engender a relatively stereotypical loading pattern resulting in a uniform distribution of loads across the joint surface; this in turn is reflected in a more highly anisotropic trabecular structure. The more isotropic trabecular structure, and possibly the more variable trabecular spacing, in the orangutan talus may reflect a more variable loading environment resulting from the diversity of positional behaviors and locomotor movements employed by members of this genus.

4.3 | Human distal femora

The analysis of the Tb.Sp z-scores for the human distal femora was able to differentiate between male and female samples. Sex-specific average color maps of Tb.Sp *z*-scores suggests that female distal femora have a region of relatively high trabecular spacing along the medial margin of the articular surface, spanning nearly the entire anteroposterior length of the medial condyle. Although a similar region can be observed in the male, the relative Tb.Sp *z*-scores are not as high in the average male. The principal component plot of Tb.Sp *z*-scores provided in Figure 11 suggests that the difference between the sexes appears to be driven by two of the male femora which separate away from the other two male specimens and all of the female distal femora along the first principal component. Larger samples of modern human distal femora could provide the ability to determine if the difference found here is representative of our species. If the pattern does characterize humans more generally, kinematic differences known to exist between men and women during both walking (Kerrigan, Todd, & Croce, 1998) and running (Ferber, McClay Davis, & Williams, 2003) may account for such structural differences.

4.4 | Sampling the entire trabecular structure

Our method could be extended to consider the entire trabecular structure of a skeletal element, both at the trabecular bone/cortical shell boundary (as presented here) and deep inside the trabecular structure of a skeletal element. The value of sliding semilandmarks and the thin-plate spline function for other types of analyses has been realized by several workers (Polly et al., 2016 and references therein), who have used the thin-plate spline function to deform a template finite element mesh to other specimens within a sample (Sigal, Hardisty, & Whyne, 2008; Stayton, 2011; Tseng, 2013). The nodes of the finite element mesh are considered sliding landmarks that are "fully relaxed" (i.e., allowed to slide in all three coordinate directions) (Neubauer, Gunz, & Hublin, 2009). If the surface of the trabecular bone/cortical shell interface were considered the external surface for sliding semilandmarks, the internal structure could be uniformly sampled with "fully relaxed" landmarks. In other words, a 3D grid of semilandmarks, anchored externally at the trabecular/cortical boundary, could be distributed throughout the trabecular structure of a skeletal element. In this way, VOIs with geometrically homologous locations could be positioned throughout the trabecular structure, allowing for more detailed comparisons of the trabecular structure between groups of interest, and could be used to isolate regions where the trabecular structure is more and less similar.

5 | CONCLUSION

Here, we demonstrate a novel technique for sampling the trabecular structure deep to the subchondral bone of articular surfaces. We demonstrate that trabecular parameters are not homogeneously distributed across the articular surface of the *Pan* and *Pongo* talus or the distal human femora. These results emphasize the necessity of analyzing multiple VOIs spread across the region of interest and may explain why prior studies utilizing only a single VOI (or a small number of VOIs) have failed to identify robust relationships between trabecular structure and behavior. Our approach is based on the geometric morphometric technique of sliding semilandmarks and allows a large number of VOIs to be automatically positioned within the trabecular structure. The strength of this approach is that, since the VOIs are consistently placed within the trabecular structure (at least in a geometric sense), statistical comparisons among groups can be made and group-specific summary statistic maps can be generated for visualization. In short, this method allows us to statistically compare groups because the VOIs are in comparable locations. This represents an advantage over other proposed methodologies that have quantified trabecular bone variation across a skeletal element, but have not been able to statistically compare individuals or groups.

ACKNOWLEDGMENTS

The authors acknowledge Dr. Dawnie Steadman and Dr. Lee Jantz for access to the μCT scans of the William M. Bass Skeletal Collection curated by the Department of Anthropology at the University of Tennessee. They also thank Dr. Doug Boyer and Dr. Erik R. Seiffert for access to scan data curated on the MorphoSource website. Two anonymous reviewers contributed to improvements in this manuscript, and they thank Peter Ellison for his editorial assistance.

REFERENCES

3D Systems Inc. (2015). *Geomagic wrap*. Rock Hill: 3D Systems Inc.

Adams, D. C., Rohlf, F. J., & Slice, D. E. (2013). A field comes of age: Geometric morphometrics in the 21st century. *Hystrix, The Italian Journal of Mammalogy*, *24*, 7–14.

Anderson, M. J., & Robinson, J. (2001). Permutation tests for linear models. *Australian & New Zealand Journal of Statistics*, *43*, 75–88.

Anselin, L., Syabri, I., & Kho, Y. (2006). GeoDa: An introduction to spatial data analysis. *Geographical Analysis*, *38*, 5–22.

Barak, M. M., Lieberman, D. E., & Hublin, J.-J. (2011). A Wolff in sheep's clothing: Trabecular bone adaptation in response to changes in joint loading orientation. *Bone*, *49*, 1141–1151.

Barak, M. M., Lieberman, D. E., Raichlen, D., Pontzer, H., Warrener, A. G., & Hublin, J.-J. (2013). Trabecular evidence for a human-like gait in *Australopithecus africanus*. *PLoS ONE*, *8*, e77687.

Bertram, J. E., & Swartz, S. M. (1991). The "law of bone transformation": A case of crying Wolff?. *Biological Reviews of the Cambridge Philosophical Society*, *66*, 245–273.

Biewener, A. A., Fazzalari, N. L., Konieczynski, D. D., & Baudinette, R. V. (1996). Adaptive changes in trabecular architecture in relation to functional strain patterns and disuse. *Bone*, *19*, 1–8.

Boyer, D. M., Gunnell, G. F., Kaufman, S., & McGeary, T. (in press). Morphosource—Archiving and sharing digital specimen data. *Journal of Paleontology*.

Boyer, D. M., & Seiffert, E. R. (2013). Patterns of astragalar fibular facet orientation in extant and fossil primates and their evolutionary implications. *American Journal of Physical Anthropology*, *151*, 420–447.

Burr, D. B., & Allen, M. R. (2014). *Basic and applied bone biology*. New York: Elsevier.

Carlson, K. J., & Patel, B. A. (2006). Habitual use of the primate forelimb is reflected in the material properties of subchondral bone in the distal radius. *Journal of Anatomy*, *208*, 659–670.

Chen, J.-H., Liu, C., You, L., & Simmons, C. A. (2010). Boning up on Wolff's Law: Mechanical regulation of the cells that make and maintain bone. *Journal of Biomechanics*, *43*, 108–118.

Chirchir, H., Kivell, T. L., Ruff, C. B., Hublin, J.-J., Carlson, K. J., Zipfel, B., & Richmond, B. G. (2015). Recent origin of low trabecular bone density in modern humans. *Proceedings of the National Academy of Sciences of United States of America*, *112*, 366–371.

Chirchir, H., Ruff, C. B., Junno, J.-A., & Potts, R. (2017). Low trabecular bone density in recent sedentary modern humans. *American Journal of Physical Anthropology*, *162*, 550–560.

Chirchir, H., Zeininger, A., Nakatsukasa, M., Ketcham, R. A., & Richmond, B. G. (in press). Does trabecular bone structure within the metacarpal heads of primates vary with hand posture? *Comptes Rendus Palevol*.

Cliff, A. D., & Ord, J. K. (1981). *Spatial processes models and applications*. London: Pion Ltd.

Collyer, M. L., Sekora, D. J., & Adams, D. C. (2015). A method for analysis of phenotypic change for phenotypes described by high-dimensional data. *Heredity*, *115*, 357–365.

Cooke, S. B., & Terhune, C. E. (2015). Form, Function, and Geometric Morphometrics. *Anatomical Records*, *298*, 5–28.

Cowin, S. C. (2001). The false premis in Wolff's law. In: S. C. Cowin (Ed.), *Bone biomechanics handbook* (2nd ed., pp. 30-1–32-5) Boca Raton: CRC Press..

Currey, J. D. (1984). *The mechanical adaptations of bones*. Princeton University Press: Princeton, NJ.

Daegling, D. J. (1992). Mandibular morphology and diet in the genusCebus. *International Journal of Primatology*, *13*, 545–570.

Daegling, D. J. (2001). Biomechanical scaling of the hominoid mandibular symphysis. *Journal of Morphology*, *250*, 12–23.

Daegling, D. J. (2007). Morphometric estimation of torsional stiffness and strength in primate mandibles. *American Journal of Physical Anthropology*, *132*, 261–266.

DeSilva, J. M., & Devlin, M. J. (2012). A comparative study of the trabecular bony architecture of the talus in humans, non-human primates, and Australopithecus. *Journal of Human Evolution*, *63*, 536–551.

Dijkstra, E. W. (1959). A note on two problems in connexion with graphs. *Numerische Mathematik*, *1*, 269–271.

Doran, D. M. (1996). Comparative positional behavior of the African apes. In W. McGrew, L. Marchant, & T Nishida (Eds.), *Great ape societies* (pp. 213–224). Cambridge: Cambridge University Press.

Doran, D. M., & Hunt, K. D. (1994). Comparative locomotor behavior of chimpanzees and bonobos: Species and habitat differences. In R. W. Wrangham, W. C. McGrew, F. B. M. de Waal, & P. G. Heltne (Eds.), *Chimpanzee cultures* (pp. 93–106.). Cambridge, MA: Harvard University Press.

Doube, M., Kłosowski, M. M., Arganda-Carreras, I., Cordelières, F. P., Dougherty, R. P., Jackson, J. S., … Shefelbine, S. J. (2010). BoneJ: Free and extensible bone image analysis in ImageJ. *Bone*, *47*, 1076–1079.

Eriksen, E. F., & Glerup, H. (2000). Pathogenesis of osteoporosis. In K. Obrant (Ed.), *Management of fractures in severely osteoporotic bone* (pp. 13–32). Springer: London.

Eriksen, E. F., Mosekilde, L., & Melsen, F. (1985). Trabecular bone remodeling and bone balance in hyperthyroidism. *Bone*, *6*, 421–428.

Fajardo, R. J., & Müller, R. (2001). Three-dimensional analysis of nonhuman primate trabecular architecture using micro-computed tomography. *American Journal of Physical Anthropology*, *115*, 327–336.

Fajardo, R. J., Müller, R., Ketcham, R. A., & Colbert, M. (2007). Nonhuman anthropoid primate femoral neck trabecular architecture and its relationship to locomotor mode. *Anatomical Records (Hoboken)*, *290*, 422–436.

FEI Visualization Sciences Group. (2015). Avizo Lite 9.0.1. Hillsboro: FEI Company.

Ferber, R., McClay Davis, I., & Williams III, D. S. (2003). Gender differences in lower extremity mechanics during running. *Clinical Biomechanics*, *18*, 350–357.

Freedman, D., & Lane, D. (1983). A Nonstochastic Interpretation of Reported Significance Levels. *Journal of Business & Economic Statistics*, *1*, 292–298.

Frost, H. M. (1987). Bone "mass" and the "mechanostat": A proposal. *Anatomical Records*, *219*, 1–9.

Frost, H. M. (1990a). Skeletal structural adaptations to mechanical usage (SATMU): 1. Redefining Wolff's law: The bone modeling problem. *Anatomical Records*, *226*, 403–413.

Frost, H. M. (1990b). Skeletal structural adaptations to mechanical usage (SATMU): 2. Redefining Wolff's law: The remodeling problem. *Anatomical Records*, *226*, 414–422.

Frost, H. M. (2003). Bone's mechanostat: A 2003 update. *The Anatomical Record Part A: Discoveries in Molecular, Cellular, & Evolutionary Biology*, *275*, 1081–1101.

Gefen, A., & Seliktar, R. (2004). Comparison of the trabecular architecture and the isostatic stress flow in the human calcaneus. *Medical Engineering & Physics*, *26*, 119–129.

Getis, A., & Aldstadt, J. (2004). Constructing the spatial weights matrix using a local statistic. *Geographical Analysis*, *36*, 90–104.

Glass, N. A., Torner, J. C., Letuchy, E. M., Burns, T. L., Janz, K. F., Eichenberger Gilmore, J. M., … Levy, S. M. (2016). The relationship between greater prepubertal adiposity, subsequent age of maturation, and bone strength during adolescence. *Journal of Bone Mineral Research*, *31*, 1455–1465.

Glatt, V., Canalis, E., Stadmeyer, L., & Bouxsein, M. L. (2007). Age-related changes in trabecular architecture differ in female and male C57BL/6J mice. *Journal of Bone Mineral Research*, *22*, 1197–1207.

Goldstein, S., Matthews, L., Kuhn, J., & Hollister, S. (1991). Trabecular bone remodeling—An experimental-model. *Journal of Biomechanics*, *24*, 135.

Griffin, N. L., D'août, K., Ryan, T. M., Richmond, B. G., Ketcham, R. A., & Postnov, A. (2010). Comparative forefoot trabecular bone architecture in extant hominids. *Journal of Human Evolution*, *59*, 202–213.

Gross, T., Kivell, T. L., Skinner, M. M., Nguyen, H., & Pahr, D. H. (2014). Holistic analysis of bone. *Palaeontologia Electronica*, *17*, 1.

Gunz, P., & Mitteroecker, P. (2013). Semilandmarks: A method for quantifying curves and surfaces. *Hystrix, The Italian Journal of Mammalogy*, *24*, 103–109.

Harcourt-Smith, W. E. H. (2003). Form and function in the hominoid tarsal skeleton. Ph.D. thesis, University of London, London, UK.

Hill, E. C., & Durband, A. C. (2014). Mobility and subsistence at the Willandra Lakes: A comparative analysis of femoral cross-sectional properties in the Lake Mungo 3 skeleton. *Journal of Human Evolution*, *73*, 103–106.

Huiskes, R., Ruimerman, R., van Lenthe, G. H., & Janssen, J. D. (2000). Effects of mechanical forces on maintenance and adaptation of form in trabecular bone. *Nature*, *405*, 704–706.

Kerrigan, D. C. M., Todd, M. K., & Croce, U. D. (1998). Gender differences in joint biomechanics during walking normative study in young adults. *Journal of Physical Medicine*, *77*, 2–7.

Kivell, T. L. (2016). A review of trabecular bone functional adaptation: What have we learned from trabecular analyses in extant hominoids and what can we apply to fossils?. *Journal of Anatomy*, *228*, 569–594.

Kivell, T. L., Skinner, M. M., Lazenby, R., & Hublin, J.-J. (2011). Methodological considerations for analyzing trabecular architecture: An example from the primate hand. *Journal of Anatomy*, *218*, 209–225.

Kuo, S., Desilva, J. M., Devlin, M. J., McDonald, G., & Morgan, E. F. (2013). The effect of the Achilles tendon on trabecular structure in the primate calcaneus. *Anatomical Records (Hoboken)*, *296*, 1509–1517.

Lanyon, L. E. (1974). Experimental support for the trajectorial theory of bone structure. *Journal of Bone & Joint Surgery*, *56B*: 160–166.

Lanyon, L. E. (1982). Mechanical function and bone remodeling. In G. Sumner-Smith (Ed.). *Bone in clinical orthopaedics* (pp. 273–304). Philadelphia: Saunders.

Lanyon, L. E. (1996). Using functional loading to influence bone mass and architecture: Objectives, mechanisms, and relationship with estrogen of the mechanically adaptive process in bone. *Bone*, *18*, 37S–43S.

Lazenby, R. A., Skinner, M. M., Kivell, T. L., & Hublin, J.-J. (2011). Scaling VOI size in 3D μCT studies of trabecular bone: A test of the oversampling hypothesis. *American Journal of Physical Anthropology*, *144*, 196–203.

Lieberman, D. E., Devlin, M. J., & Pearson, O. M. (2001). Articular area responses to mechanical loading: Effects of exercise, age, and skeletal location. *American Journal of Physical Anthropology*, *116*, 266–277.

MacLatchy, L., & Müller, R. (2002). A comparison of the femoral head and neck trabecular architecture of Galago and Perodicticus using micro-computed tomography (microCT). *Journal of Human Evolution*, *43*, 89–105.

Majumdar, S., Genant, H. K., Grampp, S., Newitt, D. C., Truong, V. H., Lin, J. C., & Mathur, A. (1997). Correlation of trabecular bone structure with age, bone mineral density, and osteoporotic status: In vivo studies in the distal radius using high resolution magnetic resonance imaging. *Journal of Bone Mineral Research*, *12*, 111–118.

Matarazzo, S. A. (2015). Trabecular architecture of the manual elements reflects locomotor patterns in primates. *PLoS ONE*, *10*, e0120436.

Mitteroecker, P., Gunz, P., Bernhard, M., Schaefer, K., & Bookstein, F. L. (2004). Comparison of cranial ontogenetic trajectories among great apes and humans. *Journal of Human Evolution*, *46*, 679–698.

Morimoto, N., Ponce de León, M. S., & Zollikofer, C. P. E. (2011). Exploring femoral diaphyseal shape variation in wild and captive chimpanzees by means of morphometric mapping: A test of Wolff's law. *Anatomical Records, (Hoboken) 294*, 589–609.

Neubauer, S., Gunz, P., & Hublin, J.-J. (2009). The pattern of endocranial ontogenetic shape changes in humans. *Journal of Anatomy*, *215*, 240–255.

Nowak, M. G., Carlson, K. J., & Patel, B. A. (2010). Apparent density of the primate calcaneo-cuboid joint and its association with locomotor mode, foot posture, and the "midtarsal break." *American Journal of Physical Anthropology*, *142*, 180–193.

Odgaard, A., & Gundersen, H. J. G. (1993). Quantification of connectivity in cancellous bone, with special emphasis on 3-D reconstructions. *Bone*, *14*, 173–182.

Pahr, D. H., & Zysset, P. K. (2009). From high-resolution CT data to finite element models: Development of an integrated modular framework. *Computer Methods in Biomechanics and Biomedical Engineering*, *12*, 45–57.

Patel, B. A., & Carlson, K. J. (2008). Apparent density patterns in subchondral bone of the sloth and anteater forelimb. *Biology Letters*, *4*, 486–489.

Patel, B. A., Ruff, C. B., Simons, E. L. R., & Organ, J. M. (2013). Humeral cross-sectional shape in suspensory primates and sloths. *Anat Rec (Hoboken)*, *296*, 545–556.

Pearson, O. M., & Lieberman, D. E. (2004). The aging of Wolff's "law": Ontogeny and responses to mechanical loading in cortical bone. *American Journal of Physical Anthropology*, *Suppl 39*, 63–99.

Polk, J. D., Blumenfeld, J., & Ahluwalia, D. (2008). Knee posture predicted from subchondral apparent density in the distal femur: An experimental validation. *Anatomical Records*, *291*, 293–302.

Polk, J. D., Williams, S. A., Peterson, J. V., Roseman, C. C., & Godfrey, L. R. (2010). Subchondral bone apparent density and locomotor behavior in extant primates and subfossil lemurs hadropithecus and pachylemur. *International Journal of Primatology*, *31*, 275–299.

Polly, P. D., Stayton, C. T., Dumont, E. R., Pierce, S. E., Rayfield, E. J., & Angielczyk, K. D. (2016). Combining geometric morphometrics and finite element analysis with evolutionary modeling: Towards a synthesis. *Journal of Vertebrate Paleontology*, *36*, e1111225.

Raggatt, L. J., & Partridge, N. C. (2010). Cellular and molecular mechanisms of bone remodeling. *Journal of Biological Chemistry*, *285*, 25103–25108.

Ridler, T. W., & Calvard, S. (1978). Picture thresholding using an iterative selection method. *Systems, Man and Cybernetics, {IEEE} Transactions on*, *8*, 630–632.

Rubin, C., Turner, A. S., Bain, S., Mallinckrodt, C., & McLeod, K. (2001). Anabolism: Low mechanical signals strengthen long bones. *Nature*, *412*, 603–604.

Ruff, C. (2008). Femoral/humeral strength in early African Homo erectus. *Journal of Human Evolution*, *54*, 383–390.

Ruff, C., Holt, B., & Trinkaus, E. (2006). Who's afraid of the big bad Wolff?: "Wolff's law" and bone functional adaptation. *American Journal of Physical Anthropology*, *129*, 484–498.

Ruff, C. B. (2002). Long bone articular and diaphyseal structure in old world monkeys and apes. I: Locomotor effects. *American Journal of Physical Anthropology*, *119*, 305–342.

Ruff, C. B., & Hayes, W. C. (1983). Cross-sectional geometry of Pecos Pueblo femora and tibiae—A biomechanical investigation: II. Sex, age, side differences. *American Journal of Physical Anthropology*, *60*, 383–400.

Ryan, T. M., Colbert, M., Ketcham, R. A., & Vinyard, C. J. (2010). Trabecular bone structure in the mandibular condyles of gouging and non-gouging platyrrhine primates. *American Journal of Physical Anthropology*, *141*, 583–593.

Ryan, T. M., & Ketcham, R. A. (2002). The three-dimensional structure of trabecular bone in the femoral head of strepsirrhine primates. *Journal of Human Evolution*, *43*, 1–26.

Ryan, T. M., & Shaw, C. N. (2012). Unique suites of trabecular bone features characterize locomotor behavior in human and non-human anthropoid primates. *Plos One*, *7*, e41037.

Ryan, T. M., & Shaw, C. N. (2013). Trabecular bone microstructure scales allometrically in the primate humerus and femur. *Proceedings of the Royal Society B: Biological Sciences*, *280*, 20130172.

Ryan, T. M., & Walker, A. (2010). Trabecular bone structure in the humeral and femoral heads of anthropoid primates. *Anatomical Records (Hoboken)*, *293*, 719–729.

Saers, J. P. P., Cazorla-Bak, Y., Shaw, C. N., Stock, J. T., & Ryan, T. M. (2016). Trabecular bone structural variation throughout the human lower limb. *Journal of Human Evolution*, *97*, 97–108.

Saparin, P., Scherf, H., Hublin, J.-J., Fratzl, P., & Weinkamer, R. (2011). Structural adaptation of trabecular bone revealed by position resolved analysis of proximal femora of different primates. *Anatomical Records (Hoboken)*, *294*, 55–67.

Scherf, H., & Tilgner, R. (2009). A new high-resolution computed tomography (CT) segmentation method for trabecular bone architectural analysis. *American Journal of Physical Anthropology*, *140*, 39–51.

Schneider, C. A., Rasband, W. S., & Eliceiri, K. W. (2012). NIH Image to ImageJ: 25 years of image analysis. *Nature Methods*, *9*, 671–675.

Sigal, I. A., Hardisty, M. R., & Whyne, C. M. (2008). Mesh-morphing algorithms for specimen-specific finite element modeling. *Journal of Biomechanics*, *41*, 1381–1389.

Skinner, M. M., Stephens, N. B., Tsegai, Z. J., Foote, A. C., Nguyen, N. H., Gross, T., … Kivell, T. L. (2015). Human-like hand use in *Australopithecus africanus*. *Science*, *347*, 395–399.

Stayton, C. T. (2011). Biomechanics on the half shell: Functional performance influences patterns of morphological variation in the emydid turtle carapace. *Zoology (Jena)*, *114*, 213–223.

Sylvester, A. D. (2013). A geometric morphometric analysis of the medial tibial condyle of African Hominids. *Anatomical Records*, *296*, 1518–1525.

Sylvester, A. D., Merkl, B. C., & Mahfouz, M. R. (2008). Assessing A.L. 288-1 femur length using computer-aided three-dimensional reconstruction. *Journal of Human Evolution*, *55*, 665–671.

Teichtahl, A. J., Wang, Y., Smith, S., Wluka, A. E., Zhu, M., Urquhart, D., … Cicuttini, F. M. (2015). Bone geometry of the hip is associated with obesity and early structural damage—A 3.0 T magnetic resonance imaging study of community-based adults. *Arthritis Research & Therapy*, *17*, 112.

Teti, A., & Zallone, A. (2009). Do osteocytes contribute to bone mineral homeostasis? Osteocytic osteolysis revisited. *Bone*, *44*, 11–16.

Toriwaki, J., & Yonekura, T. (2002). Euler number and connectivity indexes of a three dimensional digital picture. *Forma*, *17*, 183–209.

Tsegai, Z. J., Kivell, T. L., Gross, T., Nguyen, N. H., Pahr, D. H., Smaers, J. B., & Skinner, M. M. (2013). Trabecular bone structure correlates with hand posture and use in hominoids. *PLoS ONE*, *8*, e78781.

Tseng, Z. J. (2013). Testing adaptive hypotheses of convergence with functional landscapes: A case study of bone-cracking hypercarnivores. *PLoS ONE*, *8*, e65305.

Wolff, J. (1892). *Das gesetz der transformation der knochen*. Berlin: A. Hirchwild.

Woo, S. L., Kuei, S. C., Amiel, D., Gomez, M. A., Hayes, W. C., White, F. C., & Akeson, W. H. (1981). The effect of prolonged physical training on the properties of long bone: A study of Wolff's Law. *Journal of Bone & Joint Surgery: American Volume*, *63*, 780–787.

Zeininger, A., Patel, B. A., Zipfel, B., & Carlson, K. J. (2016). Trabecular architecture in the StW 352 fossil hominin calcaneus. *Journal of Human Evolution*, *97*, 145–158.

Zeininger, A., Richmond, B. G., & Hartman, G. (2011). Metacarpal head biomechanics: A comparative backscattered electron image analysis of trabecular bone mineral density in *Pan troglodytes*, *Pongo pygmaeus*, and *Homo sapiens*. *Journal of Human Evolution*, *60*, 703–710.

Zhang, Y., He, Z., Fan, S., He, K., & Li, C. (2008). Automatic Thresholding of Micro-CT Trabecular Bone Images. In: 2008 International Conference on BioMedical Engineering and Informatics. Vol. 2. pp. 23–27.

Zhou, G.-Q., Pang, Z.-H., Chen, Q.-Q., He, W., Chen, Z.-Q., Chen, L.-L., & Li, Z.-Q. (2014). Reconstruction of the biomechanical transfer path of femoral head necrosis: A subject-specific finite element investigation. *Computers in Biology and Medicine*, *52*, 96–101.

How to cite this article: Sylvester AD, Terhune CE. Trabecular mapping: Leveraging geometric morphometrics for analyses of trabecular structure. *Am J Phys Anthropol*. 2017;163:553-569. https://doi.org/10.1002/ajpa.23231